



1 **Understanding offshore high-ozone events during TRACER-AQ**
2 **2021 in Houston: Insights from WRF-CAMx photochemical**
3 **modeling**

4 Wei Li¹, Yuxuan Wang¹, Xueying Liu¹, Ehsan Soleimanian¹, Travis Griggs¹, James Flynn¹, and
5 Paul Walter²

6 ¹Department of Earth and Atmospheric Sciences, University of Houston, Houston, Texas, USA

7 ²Department of Mathematics, St. Edward's University, Austin, TX, USA

8 *Corresponding author: Yuxuan Wang (ywang246@central.uh.edu)*

9 **Abstract.** Mechanisms for high offshore ozone (O₃) events in the Houston area have not been systematically
10 examined due to limited O₃ measurements over water. In this study, we used the datasets collected by three boats
11 deployed in Galveston Bay and the Gulf of Mexico during the Tracking Aerosol Convection Interactions
12 ExpeRiment/Air Quality (TRACER-AQ) field campaign period (September 2021) in combination with the Weather
13 Research and Forecasting (WRF) coupled Comprehensive Air quality Model with Extensions (CAMx) modeling
14 system (WRF-CAMx) to investigate the reasons for high offshore O₃. The model can capture the spatiotemporal
15 variability of daytime (10:00-18:00) O₃ for the three boats (R > 0.7) but tends to overestimate O₃ by ~10 ppb on
16 clean days and underestimate O₃ by ~3 ppb during high-O₃ events. The process analysis tool in CAMx identifies O₃
17 chemistry as the major process leading to high O₃ concentrations. The region-wide increase of long-lived VOCs
18 through advection not only leads to more O₃ production under a NO_x-limited regime but also fosters VOC-limited
19 O₃ formation along western Galveston Bay and the Gulf coast under high-NO_x conditions brought by the
20 northeasterly winds from the Houston Ship Channel. Two case studies illustrate that high offshore O₃ events can
21 develop under both large- and meso-scale circulations, indicating both the regional and local emissions need to be
22 stringently controlled. Wind conditions are demonstrated to be important meteorological factors in such events, so
23 they must be well represented in photochemical models to forecast air quality over the urban coastal regions
24 accurately.

25 **1. Introduction**

26 The greater Houston area has been designated as ozone (O₃) nonattainment by U.S. Environmental Protection
27 Agency (EPA) under the National Ambient Air Quality Standards (NAAQS) standards (Nonattainment Areas for
28 Criteria Pollutants (Green Book), 2023). O₃ is a secondary criteria pollutant whose formation is non-linearly
29 dependent on the relative abundance of its precursors: volatile organic compounds and nitrogen oxides. Houston
30 experiences significant anthropogenic emissions of these precursors, mainly from transportation and petrochemical
31 facilities along the Houston Ship Channel (Leuchner and Rappenglück, 2010; Soleimanian et al., 2022). In addition,
32 due to its unique location at the land-water interface, high O₃ events in Houston are known to be related to complex



33 meteorological conditions with the interactions between synoptic and mesoscale circulations. Dry and polluted
34 continental air masses brought by northerly winds after the cold front passage are often linked with O₃ exceedances
35 (Darby, 2005; Rappenglück et al., 2008; Ngan and Byun, 2011). Extremely high O₃ can occur under a land-sea
36 breezes recirculation, in which the land breeze in the morning transports the pollution-laden air toward Galveston
37 Bay or the Gulf of Mexico, followed by the return of the aged pollutants in the afternoon by the onshore bay or sea
38 breeze (Banta et al., 2005; Caicedo et al., 2019; Li et al., 2020). Such high-O₃ events in coastal urban regions are
39 challenging for air quality models to capture as the physical and chemical processes of O₃ over both land and water
40 need to be well-constrained (Caicedo et al., 2019; Bernier et al., 2022).

41 To understand the interplay among meteorology, emissions, and chemistry, various field campaigns have been
42 deployed in the Houston area, such as the Texas Air Quality Study in 2000 and 2006 and the Deriving Information
43 on Surface Conditions from COlumn and VERTically Resolved Observations Relevant to Air Quality (DISCOVER-
44 AQ) in 2013. A common goal of these field campaigns was to evaluate the predictive ability of numerical weather
45 and air quality models using the collected observations (Misenis and Zhang, 2010; Yu et al., 2012; Li and
46 Rappenglück, 2014; Mazzuca et al., 2016; Pan et al., 2017). Although these studies greatly improve our
47 understanding of the reasons for high ozone events in Houston, they mainly focused on the onshore area due to the
48 absence of offshore measurements. Higher levels of O₃ over water bodies than the adjacent land have been observed
49 in other coastal regions with poor air quality, such as the Chesapeake Bay and Lake Michigan, due to several factors
50 including but not limited to the offshore advection of polluted air masses, photochemical productions from local
51 (e.g., marine traffic) and aged land emissions, shallow marine planetary boundary layers (PBL), the lack of NO_x
52 titration, and low dry deposition rates (Dye et al., 1995; Goldberg et al., 2014; Sullivan et al., 2019; Abdi-Oskouei et
53 al., 2022; Dreessen et al., 2023). Air quality modeling evaluations against these observations show difficulties in
54 numerical prediction of O₃ over water with an overall positive bias for low O₃ and negative bias for high O₃ due in
55 part to the misrepresentation of marine meteorology and PBL (Dreessen et al., 2019; Abdi-Oskouei et al., 2020;
56 Dacic et al., 2020; Baker et al., 2023). However, to our knowledge, high O₃ events off the Houston coast in
57 Galveston Bay and the Gulf of Mexico have not been systematically examined. The predictive ability of
58 photochemical models in capturing such events has yet to be quantified.

59 More recently, the Tracking Aerosol Convection Interactions ExpeRiment/Air Quality (TRACER-AQ) field
60 campaign revisited the Houston area in September 2021. The campaign implemented a variety of observational
61 platforms covering both offshore and onshore locations, such as stationary sites, boats, lidar, ozonesondes, and
62 airborne remote sensing. In particular, instruments onboard three boats continuously collected O₃ and
63 meteorological data from July to October over Galveston Bay and the Gulf of Mexico, which provides a valuable
64 opportunity to understand the reasons driving high O₃ concentrations over water and the O₃ non-attainment at air
65 quality monitors near the Houston coastline. Furthermore, the Texas Commission on Environmental Quality
66 (TCEQ) has created a new emission inventory for its 2019 state implementation plan (SIP) modeling platform to
67 conduct photochemical simulations using the Comprehensive Air quality Model with Extensions (CAMx) driven by
68 the Weather Research and Forecasting (WRF) meteorology. Using the established new emission inventory and



69 observations, an evaluation of offshore O₃ prediction can provide insights into model deficiencies over water and
70 help improve air quality forecasting in coastal urban regions.

71 This study aims to improve our understanding of high offshore O₃ concentrations in the Houston coastal zone during
72 the TRACER-AQ 2021 field campaign based on observations and WRF-CAMx modeling, a regulatory model used
73 by TCEQ. We first evaluate the performance of model simulations of O₃ and then investigate the reasons causing
74 high-O₃ events relative to clean days, taking advantage of the process analysis tools from CAMx. Lastly, we present
75 two case studies to better understand the development of elevated O₃ over water. Potential sources of model bias are
76 also discussed.

77 **2. Data and model setup**

78 **2.1 Meteorological and air quality observations**

79 TCEQ has O₃ and other pollutants routinely measured at the continuous ambient monitoring stations (CAMS) across
80 the Houston region. Some of these stations also observe meteorological variables, such as wind speed and direction,
81 temperature, and relative humidity (RH). These data can be downloaded from the Texas Air Monitoring Information
82 System ([TAMIS](#)) website. A commercial shrimp boat and a pontoon boat owned by the University of Houston (UH)
83 were operated mainly on the east and west sides of Galveston Bay, respectively. Another commercial boat, the Red
84 Eagle, was docked to the north of Galveston Island and typically traveled up to 90 km offshore in the Gulf of
85 Mexico and occasionally northward through the Ship Channel to the port of Houston. Automated O₃ sampling
86 instruments were installed on the three boats with a compact weather station measuring temperature, pressure, RH,
87 and wind conditions. The sample inlet was attached to an elevated location on the boats to avoid titration from the
88 boats' exhausts. Details of these devices can be found in Griggs et al. (submitted). In addition, ozonesondes were
89 launched from the pontoon and Red Eagle boats on selected days and locations to investigate the vertical O₃ profiles.
90 All the campaign data can be found on the TRACER-AQ website ([https://www-air.larc.nasa.gov/cgi-](https://www-air.larc.nasa.gov/cgi-bin/ArcView/traceraq,2021)
91 [bin/ArcView/traceraq,2021](https://www-air.larc.nasa.gov/cgi-bin/ArcView/traceraq,2021)).

92 During the offshore operational period of July to October, hourly averaged O₃ mixing ratios exceeded 100 ppb
93 several times. We identified O₃ exceedance days when offshore boat O₃ observations registered a daily maximum 8-
94 hour average (MDA8) O₃ in exceedance of 70 ppb, the current criteria of the NAAQS for O₃. Six episodes with high
95 O₃ were obtained: July 26 – 28, August 25, September 6 – 11, September 17 – 19, September 23 – 26, and October 6
96 – 9. These episodes are accompanied by at least one CAMS site exceeding the 70 ppb MDA8 O₃ threshold,
97 indicating an extensive land-water air mass interaction.

98 **2.2 WRF and CAMx model configuration**

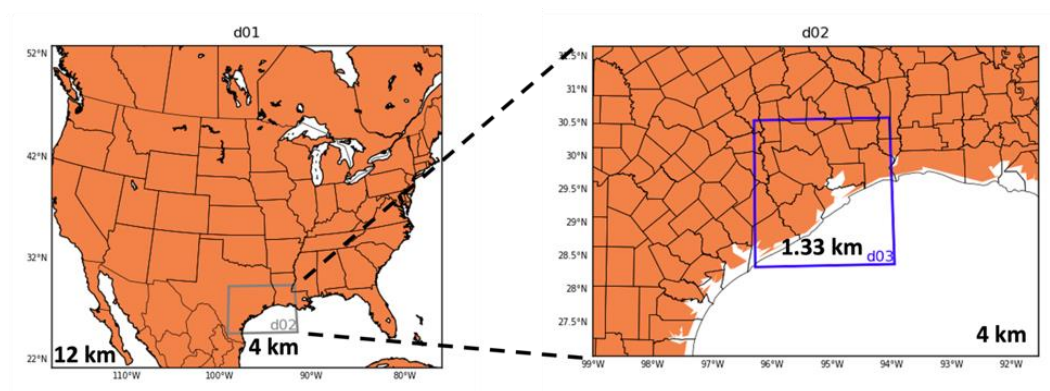
99 This study used the WRF model v3.9.1.1. We set up three domains with different horizontal resolutions that cover
100 the contiguous United States, Southeast Texas, and the Houston-Galveston-Brazoria region, referred to as domains
101 d01, d02, and d03, respectively, as shown in Figure 1. The corresponding horizontal resolutions and grid numbers



102 for d01 – d03 are 12 km × 12 km (373 × 310 grids), 4 km × 4 km (190 × 133 grids), and 1.33 km × 1.33 km (172 ×
103 184 grids), respectively. All domains have identical vertical resolutions with 50 hybrid sigma-eta vertical levels
104 spanning from the surface to 10 hPa. Boundary conditions of the two inner domains were generated from the outer
105 domain.

106 To select the WRF configurations that best represent the monitoring data, we designed eight model experiments with
107 different initial and boundary condition (IC/BC) inputs, microphysics options, PBL schemes, data assimilation
108 method (e.g., observation nudging), and reinitializing techniques. Details of the design and evaluation of each
109 experiment can be found in Liu et al. (submitted). Based on the campaign-wide evaluation of the modeled
110 meteorology, the best simulation was used to drive the CAMx model. The model configuration of the best
111 simulation includes the hourly High-Resolution Rapid Refresh (HRRR) meteorological data as IC/BC inputs, the
112 local closure Mellor-Yamada-Nakanishi-Niino (MYNN) PBL option (Nakanishi and Niino, 2009), and the Morrison
113 double moment (2M) microphysics scheme (Morrison et al., 2009) with no nudging and reinitializing techniques
114 applied. Other settings used for the WRF simulation include the Monin-Obukhov Similarity surface layer (Foken,
115 2006), the Noah land surface scheme (Chen and Dudhia, 2001), the Rapid Radiative Transfer Model (RRTM)
116 longwave and shortwave radiation schemes (Iacono et al., 2008), and the New Tiedtke cumulus parameterization
117 (Zhang et al., 2011).

118



119 **Figure 1. WRF nested modeling domains and horizontal resolutions.**

120

121 This study also used the CAMx model v7.10. The three CAMx domains aligned with the WRF grids but had smaller
122 spatial coverage. The corresponding horizontal resolutions and grid numbers for domains 1–3 are 12 km × 12 km
123 (372 × 244 grids), 4 km × 4 km (156 × 126 grids), and 1.33 km × 1.33 km (153 × 162 grids), respectively. All
124 domains have identical vertical resolutions with 30 vertical levels from the surface to ~100 hPa. The IC/BC inputs
125 for the outmost domain are from the GEOS-Chem (v12.2.1) global simulation with NEI 2011 nitrogen oxides (NO_x)
126 emissions scaled down to 2021. The Carbon Bond version 6 revision 5 (CB6r5) was used for gas-phase chemistry,



127 including the inorganic iodine depletion of O₃ over oceanic water (Burkholder et al., 2019). The first-order eddy
128 viscosity (K-theory) diffusion scheme was selected for vertical mixing within the PBL, in which the vertical
129 diffusion coefficients (K_v) were supplied from WRF outputs. Dry deposition is based on the Wesely scheme
130 (Wesely, 1989).

131 Emission files with 12 km and 4 km spatial resolutions from the preliminary 2019 SIP modeling platform provided
132 by TCEQ are used in the simulation. Since our domains are smaller than those in the SIP modeling, the original
133 emission files were cropped to match the grid boundaries for CAMx to read properly. In addition, we redistributed
134 the on-road emissions from 4 km to 1.33 km over the Houston area. The 4 km emission fluxes were first
135 disaggregated evenly to the 1.33 km grids and then collected onto major roads using a 1 km rasterized road shapefile
136 to produce on-major-road 1.33 km emissions. Some 1.33 km grid points off the major roads had missing values,
137 which were filled using a smoothing method that averaged eight nearby grid points. The scaling factors for on- and
138 off-major-road emissions were kept in order to maintain the on-road emission budget consistent before and after the
139 spatial redistribution. Finally, total emissions were calculated by adding the 1.33 km on- and off-major-road
140 emissions. The emissions for other sectors were also similarly interpolated to 1.33 km without separating into no- or
141 off-major-road temporary emissions. The redistributed emissions were tested to perform better in capturing the on-
142 road distributions than using the Flexi-nesting function in CAMx (Figure S1), which can regrid the emissions on the
143 fly.

144 The simulation was performed for two periods, July 20 – 30 and August 20 – October 13, to cover the six high-O₃
145 episodes defined in Section 2.1. A 10-day spin-up before each period was applied. Other days in the two periods are
146 considered clean scenarios with low O₃ concentrations. Process analysis, including integrated process rate analysis
147 (IPR), integrated reaction rate analysis (IRR), and chemical process analysis (CPA), was turned on when running the
148 model. IPR contains O₃ change rate from several chemical and physical processes, such as chemistry (CHEM),
149 horizontal and vertical advection (ADV) and diffusion (DIF), and deposition (DEP). IRR provides detailed
150 information about the reaction rate of all the chemical reactions in the CB6r5 scheme. CPA improves upon IRR by
151 computing parameters useful for understanding O₃ chemistry, such as O₃ production rate and regime. The O₃
152 formation regime is determined based on the ratio of hydrogen peroxide (H₂O₂) production rate from hydroperoxyl
153 radical (HO₂) self-reaction to nitric acid (HNO₃) production rate from hydroxyl radical (OH) reaction with nitrogen
154 dioxide (NO₂), in which $P(\text{H}_2\text{O}_2)/P(\text{HNO}_3) < 0.35$ indicates a VOC-limited regime and ≥ 0.35 indicates a NO_x-
155 limited regime (Sillman, 1995). There is no transition scheme available in this method.

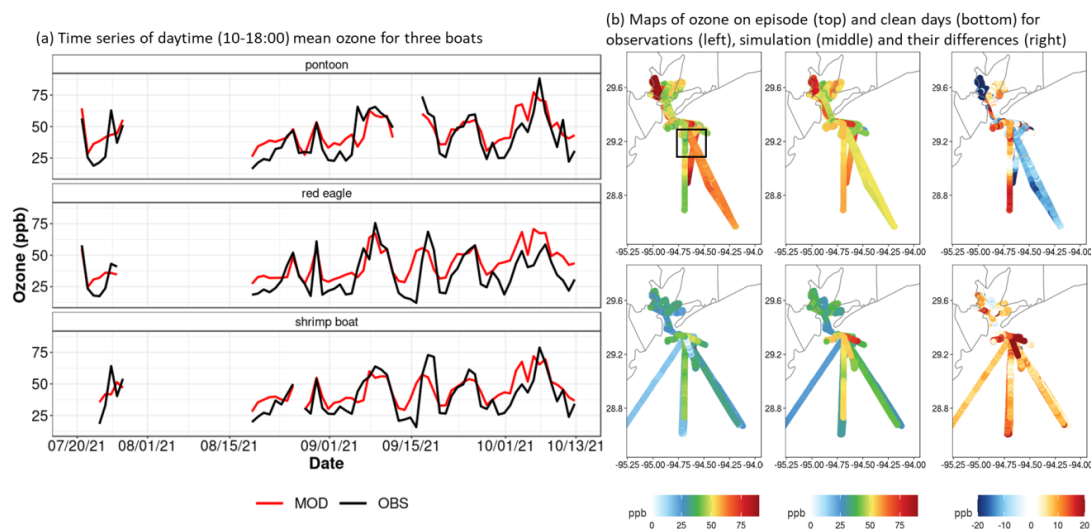
156 **3. Results**

157 **3.1 Evaluation of O₃ simulations**

158 The time series of the daytime (10:00 – 18:00) mean O₃ at the three boats are shown in Figure 2a, and the evaluation
159 statistics are listed in Table 1. The evaluation excludes nighttime data to reduce the effects from land as the boats
160 stayed at the dock at night. Indeed, an hourly time series evaluation with nighttime data included (Figure S2 and



161 Table S1) shows a larger bias between modeled ozone and boat observations. The spatiotemporal variability of
 162 daytime O₃ at the three boats is well captured by the model with a correlation coefficient (R) value greater than 0.70.
 163 Overall, the model overestimates daytime O₃ by 4.57 ppb (11%), 7.82 ppb (22%), and 4.35 ppb (9%) for the
 164 pontoon boat, Red Eagle, and shrimp boat, respectively. On episode days, high O₃ mixing ratios can be found over
 165 Galveston Bay and the Gulf of Mexico (Figure 2b). The model captures some of the variability (R=0.42 – 0.51),
 166 with negative mean bias (MB) values of ~4.5 ppb (8%) for the pontoon and shrimp boats and a nearly unbiased
 167 simulation (MB=0.05 ppb) for the Red Eagle boat. While the O₃ variability is better predicted on clean days (R=0.69
 168 – 0.76), the model shows higher values of MB than those on high-O₃ days ranging from 9.15 ppb (29%) to 11.28
 169 ppb (41%), which drives the overall model overestimation.



170
 171 **Figure 2. (a) Time series of daytime (10:00 – 18:00) mean ozone for observations at three boats (black) and simulations**
 172 **(red). (b) Maps of observed (left column), simulated (middle column), and their difference (right column) of ozone during**
 173 **ozone episodes (top row) and clean days (bottom row). The black box shows the selected offshore region for process analysis**
 174 **in the next section.**

175

176 While we did not find any previous efforts modeling offshore O₃ in the Houston area to compare our results, an
 177 evaluation against onshore measurements can help validate our model performance. The time series of the daytime
 178 mean O₃ from simulations and observations from CAMS sites are displayed in Figure 3, and the evaluation statistics
 179 are summarized in Table 2. The model captures the onshore O₃ variability (R=0.79) with an overall overestimation
 180 of 7.89 ppb (20%), mainly due to the high positive bias of 10.93 ppb (34%) on clean days. This result is comparable
 181 with the model performance from previous studies focusing on the same area (e.g., Xiao et al., 2010; Pan et al.,
 182 2015; Kommalapati et al., 2016), which further verifies the reliability of our model settings.

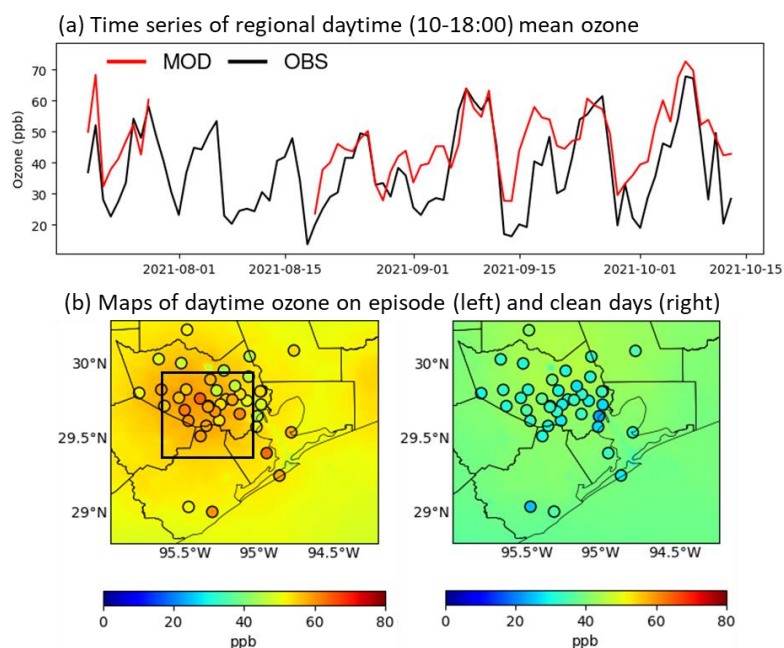
183



184 **Table 1. Daytime (10:00 – 18:00) ozone evaluation metrics at three boats, including the observed and simulated mean values,**
 185 **correlation coefficient (R), mean bias (MB), normalized mean bias (NMB), mean absolute error (MAE), and root mean square**
 186 **error (RMSE).**

Boat	Period	Observed mean (ppb)	Simulated mean (ppb)	R	MB (ppb)	NMB (%)	MAE (ppb)	RMSE (ppb)
pontoon	all days	41.18	45.76	0.77	4.57	11.12	9.75	11.57
	ozone episode	58.57	54.21	0.51	-4.36	-7.44	8.34	11.31
	clean days	32.06	41.33	0.76	9.27	28.93	10.50	11.71
Red Eagle	all days	34.86	42.69	0.71	7.82	22.45	11.15	13.42
	ozone episode	51.20	51.25	0.42	0.05	0.08	9.71	11.92
	clean days	27.60	38.88	0.69	11.28	40.89	11.80	14.03
shrimp boat	all days	39.99	44.35	0.73	4.35	10.89	9.15	11.47
	ozone episode	57.22	52.22	0.43	-5.00	-8.74	8.88	11.65
	clean days	31.17	40.32	0.69	9.15	29.36	9.28	11.38

187



188

189 **Figure 3. (a) Time series of daytime (10:00 – 18:00) mean ozone for observations at CAMS sites (OBS; black line) and**
 190 **simulations (MOD; red line). (b) Maps of observed (points) and simulated (background) daytime ozone during ozone**
 191 **episodes (left) and clean days. The black box shows the selected onshore region for process analysis in the next section.**

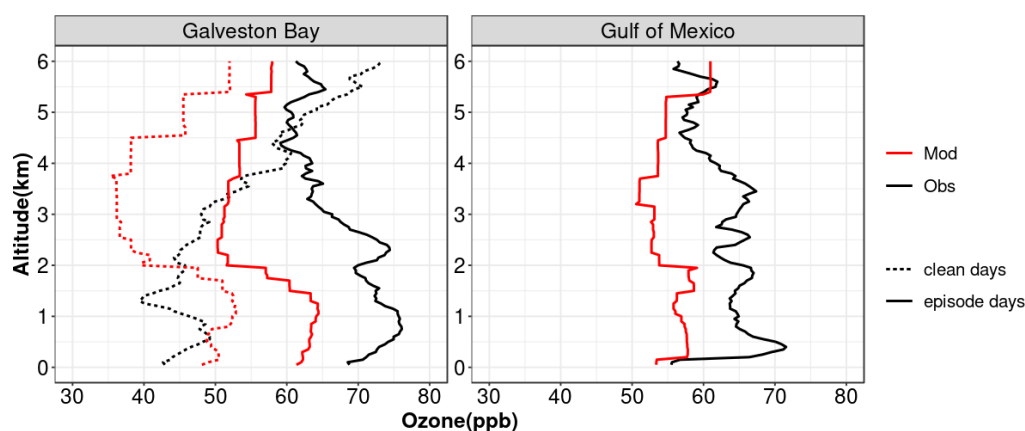
192



193 **Table 2. Daytime (10:00 – 18:00) ozone evaluation metrics at CAMS sites. The metrics are the same as in Table 1.**

Sites	Period	Observed mean (ppb)	Simulated mean (ppb)	R	MB (ppb)	NMB (%)	MAE (ppb)	RMSE (ppb)
CAMS	all days	38.87	46.76	0.79	7.89	20.32	9.41	11.72
	ozone episode	54.63	56.17	0.64	1.54	2.81	5.31	7.15
	clean days	31.34	42.28	0.64	10.93	34.88	11.35	13.37

194



195

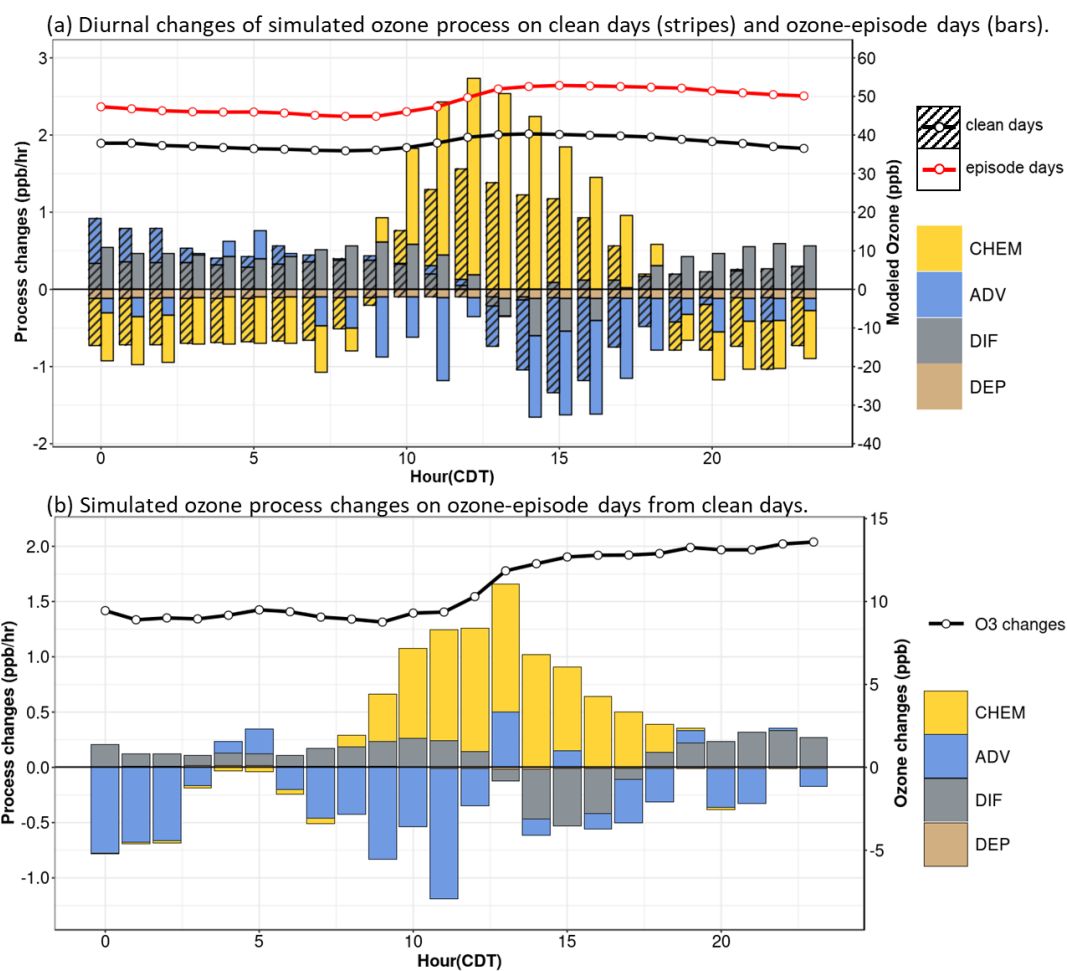
196 **Figure 4. Ozone vertical distribution from the afternoon (12:00-18:00) ozonesonde launches (Obs; black lines) and**
 197 **simulations (Mod; red lines) at Galveston Bay averaged on clean days (dashed lines) and ozone-episode days (solid lines).**
 198 **The Gulf of Mexico only sampled ozone on high-ozone days.**

199 We also evaluated the modeled vertical O₃ profiles against the afternoon (12:00-18:00) ozonesondes launched over
 200 Galveston Bay and the Gulf of Mexico. During the study period, there were five and nine afternoon launches over
 201 Galveston Bay on clean and O₃-episode days, respectively, while the Gulf of Mexico only had five afternoon
 202 launches during high-O₃ events. The average O₃ profiles from these launches are shown in Figure 4. Free
 203 tropospheric O₃ with altitudes greater than 2 km is underestimated for both locations on both clean and O₃-episode
 204 days, which indicates the long-range transported O₃ is underrepresented by the model. Over Galveston Bay, the
 205 overestimation of O₃ within the mixed layer below 2 km on clean days changes to underestimation on episode days,
 206 and the underestimation increases from 5 ppb at the surface to 10 ppb near 1 km. This underestimation of O₃ in the
 207 mixed layer on episode days can be partly explained by the missing high-O₃ layer between 2 – 3 km, which can be
 208 mixed down when the cap inversion is weak (Liu et al., submitted). There is an approximately 10 ppb
 209 underestimation across all altitudes below 4 km over the Gulf of Mexico. An ozonesonde from the Gulf of Mexico
 210 on September 9 recorded high ozone up to the top of the marine layer at 370 m, which is missed by the model and
 211 leads to the highest bias. This case will be discussed in the case study of Section 3.3.



212 To conclude, despite the overall model bias for vertical O₃ distributions, the acceptable model performance for
 213 offshore and onshore O₃ prediction at the surface indicates that the modeling system can be applied to conduct
 214 process analysis and help identify the processes influencing high O₃ concentrations over the water surface.

215 **3.2 Process analysis over the Gulf of Mexico**



216

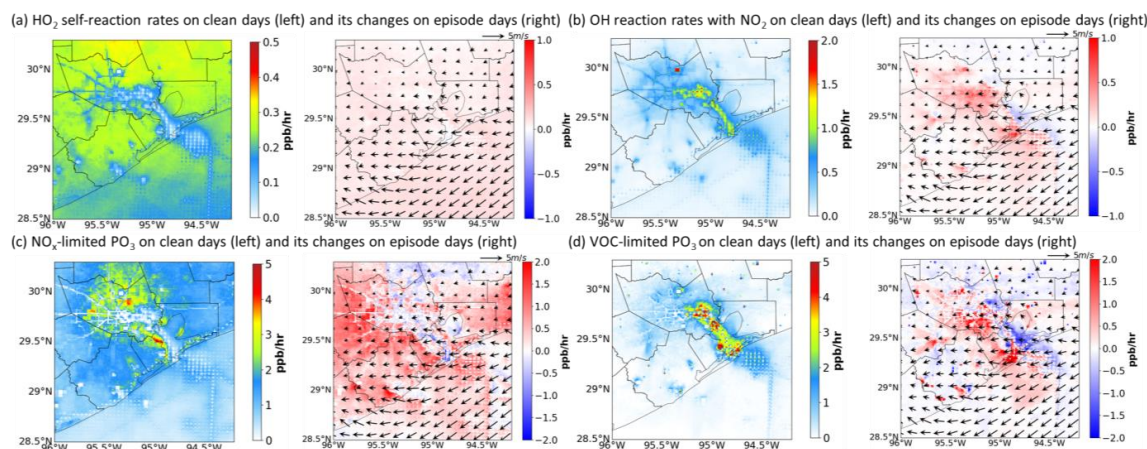
217 **Figure 5. (a) Diurnal changes of simulated ozone processes over the Gulf of Mexico (black box in Figure 2), including**
 218 **chemistry (CHEM), advection (ADV), vertical diffusion (DIF), and deposition (DEP) on clean days (stripes) and O₃-episode**
 219 **days (bars) integrated across the lowest five model layers. Overlaid lines and points are simulated hourly ozone on clean**
 220 **(black) and O₃-episode (red) days. (b) Process (filled bars) and O₃ (black line) changes during high-O₃ episodes relative to**
 221 **clean days.**

222 This section examines how the CAMx simulated O₃ processes change during high-O₃ episodes relative to clean
 223 days. The process analysis is calculated over a subregion of the Gulf of Mexico with high O₃ mixing ratios observed
 224 (black box in Figure 2b) and integrated across the lowest five model layers comparable to the morning PBL heights



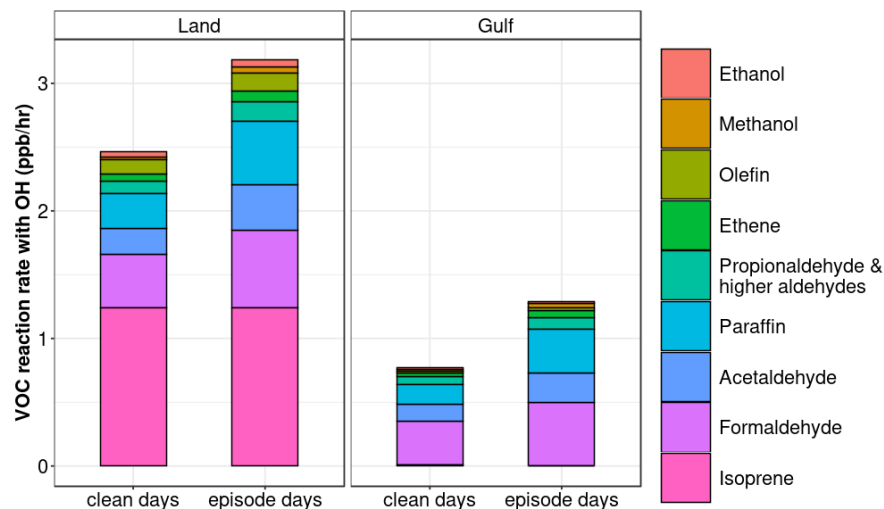
225 over water. The diurnal average of each process on clean and O₃ episode days is shown in Figure 5a. Chemistry
226 (CHEM) is the major O₃ source during daytime and becomes the primary O₃ sink after sunset. Advection (ADV)
227 serves as a pathway for an O₃ sink for most hours, especially during the day, while vertical diffusion (DIF) mostly
228 contributes as an O₃ source. Deposition (DEP) constantly removes O₃ from the atmosphere at all hours, yet with a
229 marginal value of 0.1 ppb/hr. Similar patterns can be found over the Houston urban area with a much bigger
230 magnitude (Figure S3). During high-O₃ events, CHEM is the most important process causing higher O₃ levels over
231 water relative to clean days, followed by vertical DIF (Figure 5b). We examined the simulated O₃ vertical profiles
232 and PBL heights averaged over the process analysis region on clean and episode days in Figure S4. O₃ across the
233 entire profile is higher on episode days than clean days, indicating an elevated O₃ background on high-O₃ days. In
234 addition, the O₃ gradient above and below the PBL is also higher on episode days, especially during morning hours,
235 which can induce more vertical diffusion if downmixing occurs from above the PBL when the capping inversion is
236 weak (Liu et al., submitted).

237 The CPA analysis can provide more insights into the enhanced O₃ production during high-O₃ events. We first
238 investigated the rates of HO₂ self-reaction and OH reaction with NO₂ in Figure 6a-b since they are used by the
239 model to determine the O₃ chemical regime. A region-wide increase in the HO₂ self-reaction rate leads to the
240 enhancement of PO₃ under a NO_x-limited regime (Figure 6c). Similarly, the frequency of PO₃ under a NO_x-limited
241 regime also increases regionally (Figure S5). The frequency at each grid cell is the ratio of the number of hours with
242 a greater than zero NO_x-limited PO₃ to the total midday hours (11:00 – 15:00) during the study period. HO₂ is
243 formed following the oxidation of VOCs by OH. Thus, we further compared the OH reactivity of VOCs averaged
244 from 11:00 to 15:00 on clean and episode days in Figure 7. Isoprene has the highest contribution to the total VOC
245 reactivity on the land, but its reactivity does not increase during high-O₃ events. Instead, paraffin, formaldehyde, and
246 acetaldehyde are the three VOCs experiencing the highest increase of reaction rate with OH over both land by 0.22
247 ppb/hr (84%), 0.19 ppb/hr (45%) and 0.15 ppb/hr (73%) and water by 0.18 ppb/hr (114%), 0.15 ppb/hr (44%) and
248 0.11 ppb/hr (82%), respectively, which indicates a higher contribution from regional transport on episode days as
249 they are relatively long-lived VOCs capable of traveling long distances. Indeed, the paraffin IPR analysis shows that
250 the ADV process dominates the increase of paraffin during morning hours from 06:00 to 11:00 over water (Figure
251 S6). The trajectory analysis focusing on two O₃ episodes in September shows air masses were transported from the
252 northern/central states (Soleimani et al., submitted), consistent with the wind directions demonstrated in Figure 6.
253 Such wind conditions can also bring NO_x emissions from the Houston Ship Channel downwind towards the western
254 side of Galveston Bay and the Gulf of Mexico, causing a higher OH reaction rate with NO₂ (Figure 6b) and
255 enhanced PO₃ under a VOC-limited regime (Figure 6d) therein.



256

257 **Figure 6. Maps of the rate (ppb/hr) of HO₂ self-reaction (a), OH reaction with NO₂ (b), ozone production (PO₃) under NO_x-**
 258 **limited (c) and VOC-limited (d) regimes on clean days (left) and its changes under episode days (right) during midday**
 259 **(11:00 – 15:00). Black arrows indicate the simulated wind speed and directions averaged on high-O₃ days.**



260

261 **Figure 7. OH reaction rates with different VOCs on clean days and ozone-episode days during 11:00 – 15:00 over the urban**
 262 **area (Land; black box in Figure 3) and the Gulf of Mexico (Gulf; black box in Figure 2).**

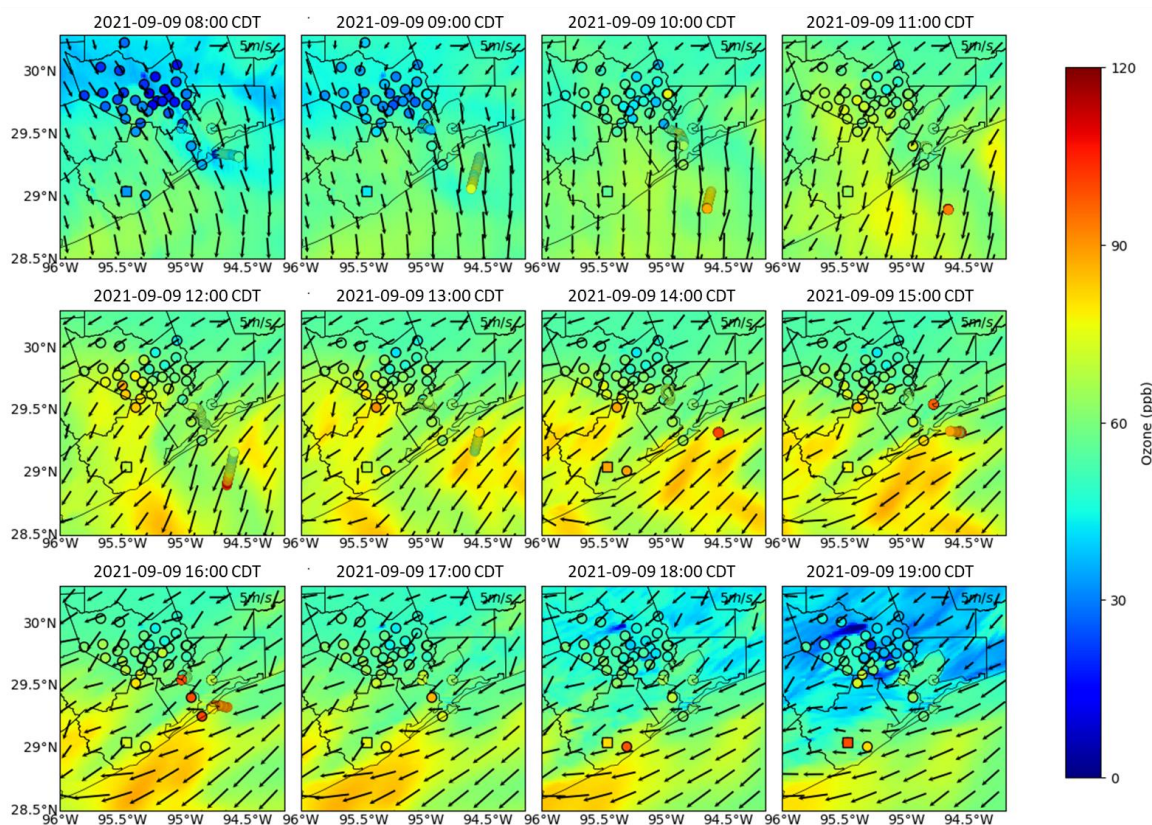
263 In summary, O₃ chemistry is the major process responsible for the high O₃ mixing ratios over the Gulf of Mexico
 264 during the study period. The VOC species with a long lifetime advected from the northeast increase over land and
 265 water, leading to a region-wide enhancement of PO₃ under a NO_x-limited regime. The downwind transport of NO_x
 266 from the Ship Channel also expands the VOC-limited area towards the west side of Galveston Bay and the Gulf of
 267 Mexico, contributing to the higher-than-normal PO₃.



268 **3.3 Case studies**

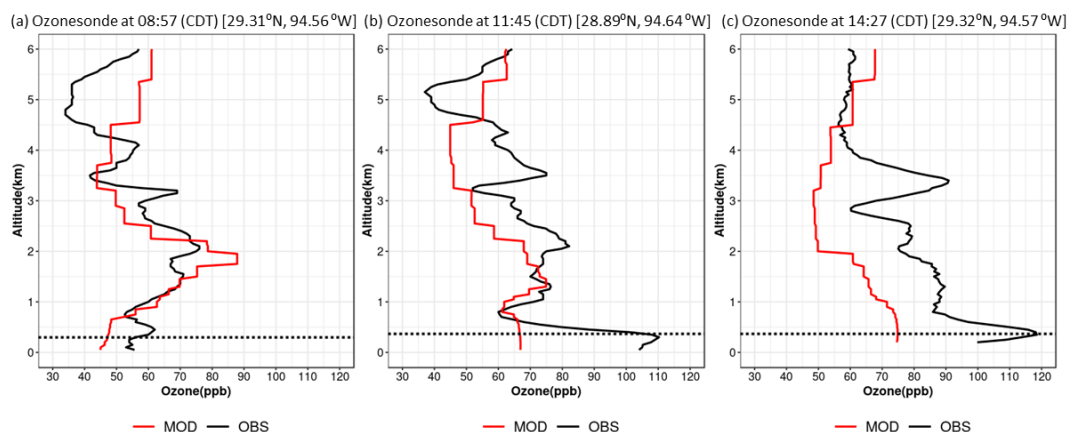
269 Although the above analysis reveals the general reasons responsible for the high offshore O₃ events, the multiple-
270 day average can miss out on some important aspects regarding the causes of these events. In this section, we selected
271 two case days, September 9 and October 7, to further demonstrate the development process of high O₃ in detail.

272 **3.3.1 Case study of September 9, 2021**



273

274 **Figure 8. Hourly simulated ozone distributions (color contours) from 08:00 to 19:00 (CDT) on September 9 overlaid with**
275 **winds (arrows). Onshore and offshore dots indicate ozone from CAMS sites and boat observations. The square mark**
276 **highlights the Lake Jackson CAMS site.**



277

278 **Figure 9. Ozone vertical profiles from ozonesondes (black line) and model simulations (red line) at 08:57 (a), 11:45 (b), and**
 279 **14:27 (c) on September 9. Black dash lines indicate the observed boundary layer height.**

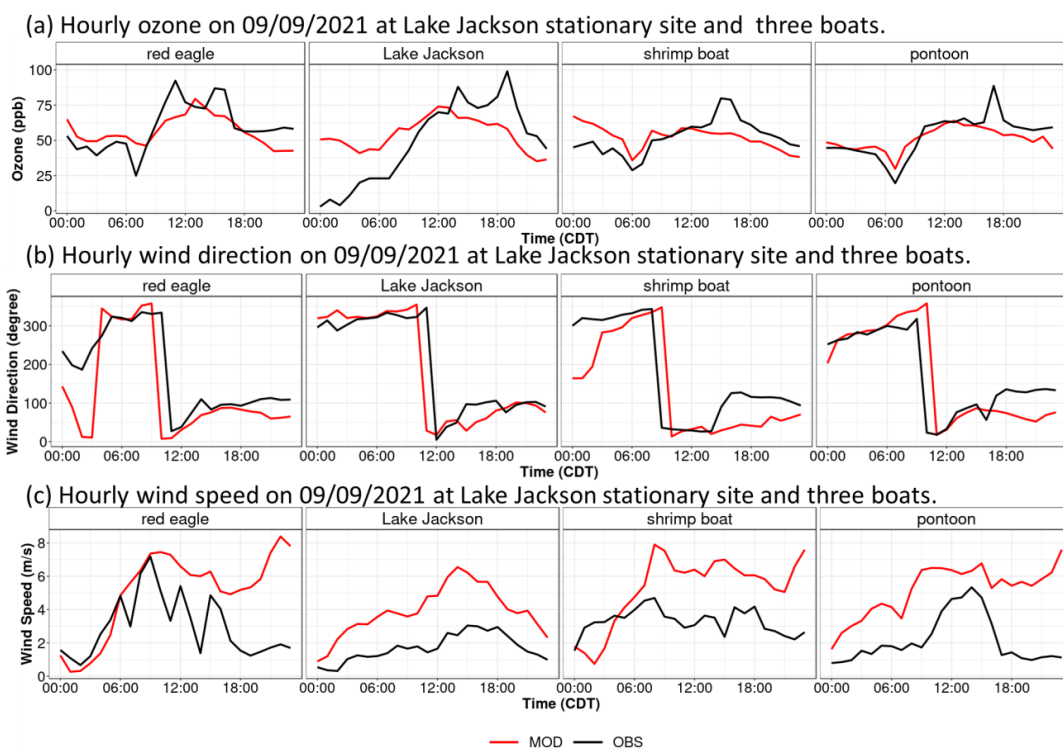
280 Multiple CAMS sites exceeded the 70 ppb MDA8 O₃ standard on September 9, with the Red Eagle boat sampling
 281 the up to 115 ppb 1-minute O₃ in the Gulf of Mexico off the coast of Galveston Island. The hourly progression of the
 282 observed and simulated O₃ is displayed in Figure 8, overlaid with modeled winds. In the morning, the study area
 283 was dominated by northerly winds bringing the fresh emissions offshore while the pontoon boat was sampling over
 284 the west side of Galveston Bay and the Red Eagle boat was traveling in the Gulf of Mexico off the coast of
 285 Galveston Island. The ozonesonde launched near 09:00 shows a moderate level of O₃ (~55 ppb) below the shallow
 286 marine boundary layer of 200 m overlaid by a residual layer with a maximum O₃ mixing ratio of 63 ppb at ~500 m
 287 (Figure 9a). Around 11:00-12:00, with high solar radiation, the seaward-transported emissions formed O₃ through
 288 photochemical reactions over water, which was captured by the Red Eagle boat with an hourly peak O₃ mixing ratio
 289 of 92 ppb (Figure 10a). Correspondingly, the O₃ vertical profile from the 11:45 balloon launch at the Red Eagle deck
 290 recorded the highest O₃ of 110 ppb at ~315 m (Figure 9b).

291 However, the model missed these peak values because the simulated wind speed is up to 4 m/s higher than
 292 observations (Figure 10c), making the plume advect faster. This also leads to a two-hour earlier arrival of the
 293 modeled O₃ peak at the Lake Jackson coastal site (square mark in Figure 8) than the observed first peak at 14:00
 294 (Figure 10a). At the same time, another plume was brought into the Gulf of Mexico from the east boundary of the
 295 domain as the wind directions changed from north to east. As the Red Eagle boat steered back to Galveston Island,
 296 all three boats sampled this plume at 14:00-17:00, resulting in the second O₃ peak at the Red Eagle boat and the only
 297 O₃ peak at the other two boats. The ozonesonde launched at 14:27 from the Red Eagle boat (Figure 9c) observed O₃
 298 reaching 118 ppb in the plume at ~370 m. This plume was continuously transported southwestward and reached the
 299 Lake Jackson site at 19:00, producing a second O₃ peak. Due to the overestimated wind speed and the simulated
 300 wind direction not completely veering to the east as observations (about 100° in Figure 10b), the model failed to
 301 predict the timing and the magnitude of the O₃ peaks caused by the second plume. The process analysis on this day
 302 over the Gulf of Mexico (black box in Figure 2) shows ADV, in addition to CHEM, contributes to the enhanced O₃



303 levels at 10:00 and 13:00 (Figure S7), which respectively corresponds to the two plumes under northerly and
 304 easterly winds and highlights the importance of regional transport. This also demonstrates that the contributions
 305 from ADV to the increase of O₃ can be high on some specific cases, which can be averaged out in our composite
 306 analysis of Figure 5.

307



308

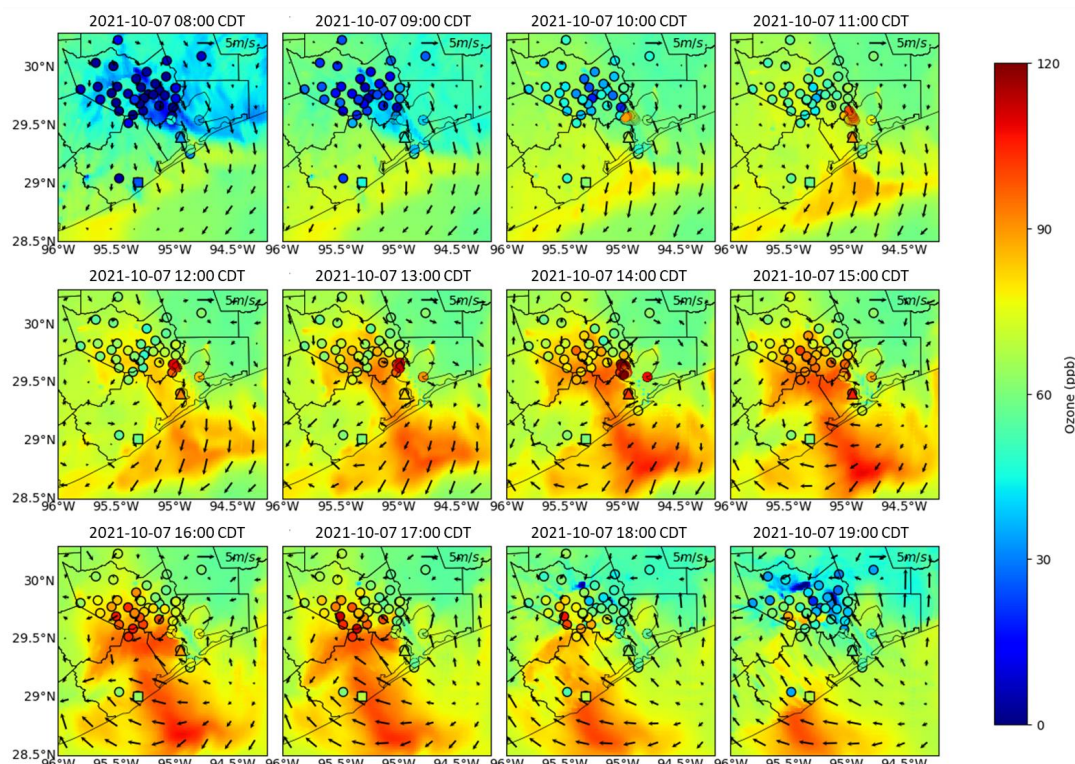
309 **Figure 10. Hourly ozone (a), wind direction (b), and wind speed (c) on September 9 from observations at the Lake Jackson**
 310 **CAMS site (square mark in Figure 8) and three boats (black) in comparison with model simulations (red).**

311

312 In summary, the wind direction changes from the north to the east on September 9 caused two O₃ peaks, as captured
 313 by the Red Eagle boat and the Lake Jackson site. This corresponds to the two simulated ozone plumes shown in the
 314 maps. One plume is produced locally and the other is transported from the eastern boundary of the domain. The
 315 model overestimates the wind speed, and the simulated wind direction does not change entirely to easterly, leading
 316 to lower or totally missed and temporally mismatched O₃ peaks relative to observations.



317 **3.3.2 Case study of October 7, 2021**



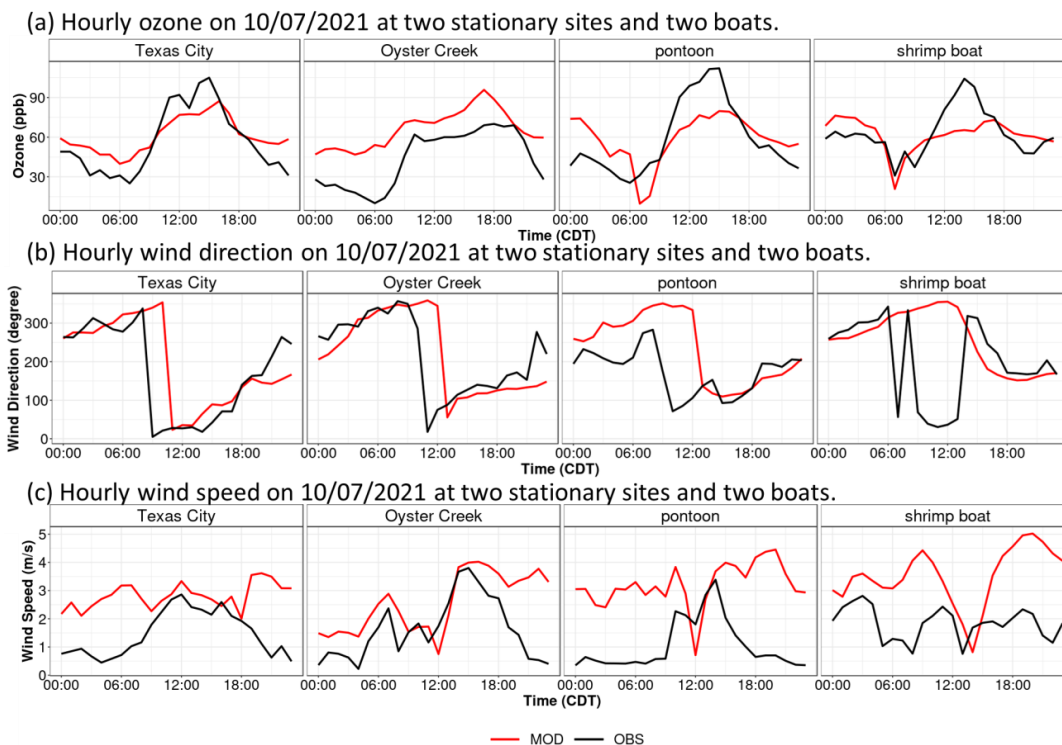
318

319 **Figure 11. Same as Figure 8 but on October 7 with the square and triangle marks representing the Oyster Creek and Texas**
 320 **City CAMS sites, respectively.**

321 On October 7, the pontoon boat observed the highest one-minute O₃ concentration (135 ppb) throughout the entire
 322 campaign period. This day started with weak northwesterly winds in the morning under post-frontal conditions,
 323 leading to high O₃ concentrations along the Gulf coast (Figure 11). The winds transitioned to northeasterly near
 324 11:00 (Figure 12b), marking the onset of the Galveston Bay breeze at the pontoon and shrimp boat and the Texas
 325 City site (triangle label in Figure 11) and the Gulf breeze at the Oyster Creek site (square label in Figure 11), both
 326 accompanied by an increase of O₃ (Figure 12a) and wind speed (Figure 12c). By contrast, the model predicted a late
 327 onset of the Bay/Gulf breezes by two to three hours with a generally higher wind speed than was observed.
 328 Afterward, the wind directions further shifted to the east to southeast between 14:00 to 18:00 as the Gulf breezes
 329 propagated to all four locations in Figure 12b, causing the highest O₃ mixing ratios therein. Similarly, the model
 330 overestimated the Gulf breeze intensity, leading to the underestimation of O₃ at the three locations along Galveston
 331 Bay. The model also continuously overestimated the moderate level of O₃ (60-70 ppb) at the Oyster Creek site under
 332 the Gulf breeze from 11:00 to 20:00, implying that the lifetime of O₃ or its precursors over water was likely
 333 overpredicted. Different from September 9, the process analysis on this local-scale event indicates CHEM is the
 334 major process leading to high O₃ concentrations over the Gulf of Mexico (Figure S8). ADV only contributes to the



335 increase of O_3 at 08:00-09:00, corresponding to the offshore transport of O_3 in the morning under northwesterly
 336 winds.



337

338 **Figure 12.** Same as Figure 10 but on October 7 with the Texas City (triangle mark in Figure 11) and Oyster Creek (square
 339 mark in Figure 11) CAMS sites and two boats.

340

341 To sum up, the high O_3 event on October 7 was related to the mesoscale Galveston Bay and Gulf breeze
 342 recirculation. Two boats and the Texas City site captured the start of the Bay breeze at ~11:00 and the development
 343 of the Gulf breeze at 14:00 – 18:00, the latter of which leads to peak hourly O_3 by bringing the aged O_3 and
 344 emissions back to land. Affected continuously by the Gulf breeze from 11:00 to 20:00, O_3 at the Oyster Creek site
 345 stayed at 60 – 70 ppb. The model predicts the onset of the Bay and Gulf breezes two to three hours late with higher
 346 wind speed, causing the delayed and lower O_3 peaks along Galveston Bay.

347 4 Conclusions

348 As part of the TRACER-AQ 2021 field campaign in the Houston area, three boats, a UH pontoon boat and two
 349 commercial vessels, equipped with an automatic sampling system and ozonesonde launches were deployed in
 350 Galveston Bay and the Gulf of Mexico from July to October. The resulting datasets, including the surface and



351 vertical O₃ concentrations and various meteorological parameters, provide a unique opportunity to evaluate the
352 performance of TCEQ's regulatory WRF-CAMx modeling system regarding its ability to capture the high offshore
353 O₃ events. Driven by the optimized WRF meteorological outputs, the CAMx model can satisfactorily capture the
354 spatiotemporal variability of daytime O₃ for the three boats ($R > 0.70$) with an overall 4 – 8 ppb (9% – 22%)
355 overestimation mainly caused by the high positive biases on clean days. During high-O₃ events, the model tends to
356 underestimate O₃ by 5 ppb near the surface and by 10 ppb up to 4 km aloft.

357 The reasonable model performance provides credibility for relying on the model's process analysis tool to
358 investigate the factors responsible for the high-O₃ episodes over the Gulf of Mexico. The results show that O₃
359 chemistry is the major process leading to high O₃ concentrations relative to clean conditions. A region-wide increase
360 of long-lived VOC species through advection, such as paraffin, formaldehyde, and acetaldehyde, accelerated O₃
361 production rates under a NO_x-limited regime. In the meantime, the enhanced VOCs can produce more O₃ near
362 western Galveston Bay and off the Gulf coast under high-NO_x concentrations brought by the northeasterly winds
363 from the Houston Ship Channel. Thus, the higher O₃ chemical production over water can be from both NO_x- and
364 VOC-limited regimes.

365 Two cases, September 9 and October 7, were then selected to illustrate the development of high-O₃ events further.
366 Both cases involved north/northeast morning winds transporting the inland emissions toward the sea, shifting to the
367 east/southeast in the afternoon, and transporting the offshore O₃ and its precursors to the land. Therefore, well-
368 represented wind conditions are of great importance for air quality models to accurately capture the timing and
369 magnitude of elevated O₃ levels in these cases. However, the two cases differ in terms of atmospheric scale. The
370 event on September 9 was influenced by a large-scale circulation with regionally homogeneous wind conditions.
371 The easterly winds in the afternoon brought a second air plume from the eastern boundary of the domain following
372 the first locally produced plume, illustrating the contributions of regional advection, in addition to chemistry, to the
373 high O₃ mixing ratios in this case. Conversely, the October 7 case was dominated by the mesoscale development of
374 Bay and Gulf breezes, characterized by a generally lower wind speed and higher O₃ level. Double O₃ peaks can also
375 be observed near Galveston Bay, such as the Texas City site in this case, corresponding to the arrival of the Bay and
376 Gulf breezes, respectively. The model mispredicted the timing of the wind direction shift and overestimated the
377 wind speed in both cases, leading to the temporally mismatched and numerically buffered O₃ peaks.

378 This study reveals the important role of chemical O₃ production over Galveston Bay and the Gulf of Mexico from
379 precursors emitted from adjacent land and the Ship Channel or transported regionally from the northeastern states.
380 The high O₃ produced offshore can then be transported back to land and cause O₃ exceedances at the air quality
381 monitors. Therefore, local and regional emissions need to be stringently regulated to reduce the frequency of such
382 events. Additionally, wind conditions are critical meteorological factors leading to these high-O₃ episodes and thus
383 need to be well represented in photochemical models to have an accurate air quality forecast in urban coastal
384 regions.



385 **Acknowledgments**

386 This research was supported by the Texas Commission for Environmental Quality (TCEQ, Grant Numbers 582-22-
387 31544-019) and the State of Texas Air Quality Research Program (AQRP, Project 20-008). The findings, opinions,
388 and conclusions are the work of the author(s) and do not necessarily represent the findings, opinions, or conclusions
389 of the TCEQ or AQRP. We acknowledge the individuals and groups who collected and shared the TRACER-AQ
390 2021 filed campaign datasets.

391 **Data Availability**

392 CAMx and WRF models are publicly available at <https://www.camx.com/> and
393 https://www2.mmm.ucar.edu/wrf/users/download/get_source.html, respectively. CAMS data can be downloaded
394 from the TAMIS web interface (<https://www17.tceq.texas.gov/tamis/index.cfm?fuseaction=home.welcome>), and
395 other campaign data is archived in the TRACER-AQ website ([https://www-air.larc.nasa.gov/cgi-
396 bin/ArcView/traceraq.2021](https://www-air.larc.nasa.gov/cgi-bin/ArcView/traceraq.2021)).

397 **Competing interests**

398 The authors declare that they have no conflict of interest.

399 **Author contributions**

400 YW conceived the research idea. WL, XL and ES conducted the model simulation. TG, JF and PW provided the
401 field observations. WL performed the data analysis and drafted the initial manuscript. All authors contributed to the
402 interpretation of the results and the preparation of the manuscript

403 **References**

- 404 Abdi-Oskouei, M., Carmichael, G., Christiansen, M., Ferrada, G., Roozitalab, B., Sobhani, N., Wade, K.,
405 Czarnetzki, A., Pierce, R. B., Wagner, T., and Stanier, C.: Sensitivity of Meteorological Skill to Selection of WRF-
406 Chem Physical Parameterizations and Impact on Ozone Prediction During the Lake Michigan Ozone Study
407 (LMOS), *J. Geophys. Res. Atmospheres*, 125, e2019JD031971, <https://doi.org/10.1029/2019JD031971>, 2020.
- 408 Abdi-Oskouei, M., Roozitalab, B., Stanier, C. O., Christiansen, M., Pfister, G., Pierce, R. B., McDonald, B. C.,
409 Adelman, Z., Janseen, M., Dickens, A. F., and Carmichael, G. R.: The Impact of Volatile Chemical Products, Other
410 VOCs, and NO_x on Peak Ozone in the Lake Michigan Region, *J. Geophys. Res. Atmospheres*, 127,
411 e2022JD037042, <https://doi.org/10.1029/2022JD037042>, 2022.
- 412 Baker, K. R., Liljegren, J., Valin, L., Judd, L., Szykman, J., Millet, D. B., Czarnetzki, A., Whitehill, A., Murphy, B.,
413 and Stanier, C.: Photochemical model representation of ozone and precursors during the 2017 Lake Michigan ozone
414 study (LMOS), *Atmos. Environ.*, 293, 119465, <https://doi.org/10.1016/j.atmosenv.2022.119465>, 2023.
- 415 Banta, R. M., Senff, C. J., Nielsen-Gammon, J., Darby, L. S., Ryerson, T. B., Alvarez, R. J., Sandberg, S. P.,
416 Williams, E. J., and Trainer, M.: A Bad Air Day in Houston, *Bull. Am. Meteorol. Soc.*, 86, 657–670,
417 <https://doi.org/10.1175/BAMS-86-5-657>, 2005.



- 418 Bernier, C., Wang, Y., Gronoff, G., Berkoff, T., Knowland, K. E., Sullivan, J. T., Delgado, R., Caicedo, V., and
419 Carroll, B.: Cluster-based characterization of multi-dimensional tropospheric ozone variability in coastal regions: an
420 analysis of lidar measurements and model results, *Atmospheric Chem. Phys.*, 22, 15313–15331,
421 <https://doi.org/10.5194/acp-22-15313-2022>, 2022.
- 422 Burkholder, J. B., Sander, S. P., Abbatt, J. P. D. A. D., Barker, J. R., Huie, R. E., Kolb, C. E., Iii, M. J. K., Orkin, V.
423 L., Wilmouth, D. M., and Wine, P. H.: Chemical Kinetics and Photochemical Data for Use in Atmospheric Studies:
424 Evaluation number 18, JPL Publ. 15-10, Jet Propulsion Laboratory, Pasadena, CA, 2019.
- 425 Caicedo, V., Rappenglueck, B., Cuchiara, G., Flynn, J., Ferrare, R., Scarino, A. J., Berkoff, T., Senff, C., Langford,
426 A., and Lefer, B.: Bay Breeze and Sea Breeze Circulation Impacts on the Planetary Boundary Layer and Air Quality
427 From an Observed and Modeled DISCOVER-AQ Texas Case Study, *J. Geophys. Res. Atmospheres*, 124, 7359–
428 7378, <https://doi.org/10.1029/2019JD030523>, 2019.
- 429 Chen, F. and Dudhia, J.: Coupling an Advanced Land Surface–Hydrology Model with the Penn State–NCAR MM5
430 Modeling System. Part I: Model Implementation and Sensitivity, *Mon. Weather Rev.*, 129, 569–585,
431 [https://doi.org/10.1175/1520-0493\(2001\)129<0569:CAALSH>2.0.CO;2](https://doi.org/10.1175/1520-0493(2001)129<0569:CAALSH>2.0.CO;2), 2001.
- 432 Dacic, N., Sullivan, J. T., Knowland, K. E., Wolfe, G. M., Oman, L. D., Berkoff, T. A., and Gronoff, G. P.:
433 Evaluation of NASA’s high-resolution global composition simulations: Understanding a pollution event in the
434 Chesapeake Bay during the summer 2017 OWLETS campaign, *Atmos. Environ.*, 222, 117133,
435 <https://doi.org/10.1016/j.atmosenv.2019.117133>, 2020.
- 436 Darby, L. S.: Cluster Analysis of Surface Winds in Houston, Texas, and the Impact of Wind Patterns on Ozone, *J.*
437 *Appl. Meteorol. Climatol.*, 44, 1788–1806, <https://doi.org/10.1175/JAM2320.1>, 2005.
- 438 Dreessen, J., Orozco, D., Boyle, J., Szyborski, J., Lee, P., Flores, A., and Sakai, R. K.: Observed ozone over the
439 Chesapeake Bay land-water interface: The Hart-Miller Island Pilot Project, *J. Air Waste Manag. Assoc.*, 69, 1312–
440 1330, <https://doi.org/10.1080/10962247.2019.1668497>, 2019.
- 441 Dreessen, J., Ren, X., Gardner, D., Green, K., Stratton, P., Sullivan, J. T., Delgado, R., Dickerson, R. R., Woodman,
442 M., Berkoff, T., Gronoff, G., and Ring, A.: VOC and trace gas measurements and ozone chemistry over the
443 Chesapeake Bay during OWLETS-2, 2018, *J. Air Waste Manag. Assoc.*, 73, 178–199,
444 <https://doi.org/10.1080/10962247.2022.2136782>, 2023.
- 445 Dye, T. S., Roberts, P. T., and Korc, M. E.: Observations of Transport Processes for Ozone and Ozone Precursors
446 during the 1991 Lake Michigan Ozone Study, *J. Appl. Meteorol. Climatol.*, 34, 1877–1889,
447 [https://doi.org/10.1175/1520-0450\(1995\)034<1877:OOTPFO>2.0.CO;2](https://doi.org/10.1175/1520-0450(1995)034<1877:OOTPFO>2.0.CO;2), 1995.
- 448 Nonattainment Areas for Criteria Pollutants (Green Book): <https://www.epa.gov/green-book>, last access: 6 January
449 2023.
- 450 Foken, T.: 50 Years of the Monin–Obukhov Similarity Theory, *Bound.-Layer Meteorol.*, 119, 431–447,
451 <https://doi.org/10.1007/s10546-006-9048-6>, 2006.
- 452 Goldberg, D. L., Loughner, C. P., Tzortziou, M., Stehr, J. W., Pickering, K. E., Marufu, L. T., and Dickerson, R. R.:
453 Higher surface ozone concentrations over the Chesapeake Bay than over the adjacent land: Observations and models
454 from the DISCOVER-AQ and CBODAQ campaigns, *Atmos. Environ.*, 84, 9–19,
455 <https://doi.org/10.1016/j.atmosenv.2013.11.008>, 2014.
- 456 Griggs, T., Flynn, J., Wang, Y., Alvarez, S., Comas, M., and Walter, P.: Characterizing Over-Water High Ozone
457 Events in the Houston-Galveston-Brazoria Region During July-October 2021, *Bull. Am. Meteorol. Soc.*, submitted.



- 458 Iacono, M. J., Delamere, J. S., Mlawer, E. J., Shephard, M. W., Clough, S. A., and Collins, W. D.: Radiative forcing
459 by long-lived greenhouse gases: Calculations with the AER radiative transfer models, *J. Geophys. Res.*
460 *Atmospheres*, 113, <https://doi.org/10.1029/2008JD009944>, 2008.
- 461 Kommalapati, R. R., Liang, Z., and Huque, Z.: Photochemical model simulations of air quality for Houston–
462 Galveston–Brazoria area and analysis of ozone–NO_x–hydrocarbon sensitivity, *Int. J. Environ. Sci. Technol.*, 13,
463 209–220, <https://doi.org/10.1007/s13762-015-0862-6>, 2016.
- 464 Leuchner, M. and Rappenglück, B.: VOC source–receptor relationships in Houston during TexAQS-II, *Atmos.*
465 *Environ.*, 44, 4056–4067, <https://doi.org/10.1016/j.atmosenv.2009.02.029>, 2010.
- 466 Li, W., Wang, Y., Bernier, C., and Estes, M.: Identification of Sea Breeze Recirculation and Its Effects on Ozone in
467 Houston, TX, During DISCOVER-AQ 2013, *J. Geophys. Res. Atmospheres*, 125, e2020JD033165,
468 <https://doi.org/10.1029/2020JD033165>, 2020.
- 469 Li, X. and Rappenglück, B.: A WRF–CMAQ study on spring time vertical ozone structure in Southeast Texas,
470 *Atmos. Environ.*, 97, 363–385, <https://doi.org/10.1016/j.atmosenv.2014.08.036>, 2014.
- 471 Liu, X., Wang, Y., Wasti, S., Li, W., Soleimanian, E., Flynn, J., Griggs, T., Alvarez, S., Sullivan, J. T., Roots, M.,
472 Gronoff, G., Berkoff, T., Walter, P., Estes, M., Hair, J. W., Shingler, T., Jo Scarino, A., Fenn, M., and Judd, L.:
473 Evaluating WRF–GC v2.0 predictions of boundary layer and vertical ozone profiles during the 2021 TRACER–AQ
474 campaign in Houston, Texas, *Geosci. Model Dev.*, submitted.
- 475 Mazzuca, G. M., Ren, X., Loughner, C. P., Estes, M., Crawford, J. H., Pickering, K. E., Weinheimer, A. J., and
476 Dickerson, R. R.: Ozone production and its sensitivity to NO_x and VOCs: results from the DISCOVER–AQ field
477 experiment, Houston 2013, *Atmospheric Chem. Phys.*, 16, 14463–14474, [https://doi.org/10.5194/acp-16-14463-](https://doi.org/10.5194/acp-16-14463-2016)
478 2016, 2016.
- 479 Misenis, C. and Zhang, Y.: An examination of sensitivity of WRF/Chem predictions to physical parameterizations,
480 horizontal grid spacing, and nesting options, *Atmospheric Res.*, 97, 315–334,
481 <https://doi.org/10.1016/j.atmosres.2010.04.005>, 2010.
- 482 Morrison, H., Thompson, G., and Tatarskii, V.: Impact of Cloud Microphysics on the Development of Trailing
483 Stratiform Precipitation in a Simulated Squall Line: Comparison of One- and Two-Moment Schemes, *Mon. Weather*
484 *Rev.*, 137, 991–1007, <https://doi.org/10.1175/2008MWR2556.1>, 2009.
- 485 Nakanishi, M. and Niino, H.: Development of an Improved Turbulence Closure Model for the Atmospheric
486 Boundary Layer, *J. Meteorol. Soc. Jpn. Ser II*, 87, 895–912, <https://doi.org/10.2151/jmsj.87.895>, 2009.
- 487 Ngan, F. and Byun, D.: Classification of Weather Patterns and Associated Trajectories of High-Ozone Episodes in
488 the Houston–Galveston–Brazoria Area during the 2005/06 TexAQS-II, *J. Appl. Meteorol. Climatol.*, 50, 485–499,
489 <https://doi.org/10.1175/2010JAMC2483.1>, 2011.
- 490 Pan, S., Choi, Y., Roy, A., Li, X., Jeon, W., and Souri, A. H.: Modeling the uncertainty of several VOC and its
491 impact on simulated VOC and ozone in Houston, Texas, *Atmos. Environ.*, 120, 404–416,
492 <https://doi.org/10.1016/j.atmosenv.2015.09.029>, 2015.
- 493 Pan, S., Choi, Y., Roy, A., and Jeon, W.: Allocating emissions to 4 km and 1 km horizontal spatial resolutions and
494 its impact on simulated NO_x and O₃ in Houston, TX, *Atmos. Environ.*, 164, 398–415,
495 <https://doi.org/10.1016/j.atmosenv.2017.06.026>, 2017.
- 496 Rappenglück, B., Perna, R., Zhong, S., and Morris, G. A.: An analysis of the vertical structure of the atmosphere and
497 the upper-level meteorology and their impact on surface ozone levels in Houston, Texas, *J. Geophys. Res.*
498 *Atmospheres*, 113, <https://doi.org/10.1029/2007JD009745>, 2008.



- 499 Sillman, S.: The use of NO_y, H₂O₂, and HNO₃ as indicators for ozone-NO_x-hydrocarbon sensitivity in urban
500 locations, *J. Geophys. Res. Atmospheres*, 100, 14175–14188, <https://doi.org/10.1029/94JD02953>, 1995.
- 501 Soleimanian, E., Wang, Y., and Estes, M.: Long-term trend in surface ozone in Houston-Galveston-Brazoria:
502 Sectoral contributions based on changes in volatile organic compounds, *Environ. Pollut.*, 308, 119647,
503 <https://doi.org/10.1016/j.envpol.2022.119647>, 2022.
- 504 Soleimanian, E., Wang, Y., Li, W., Liu, X., Griggs, T., Flynn, J., Walter, P., and Estes, M.: Understanding Ozone
505 Episodes during the TRACER-AQ Campaign in Houston, Texas: The Role of Transport and Ozone Production
506 Sensitivity to Precursors, *Sci. Total Environ.*, submitted.
- 507 Sullivan, J. T., Berkoff, T., Gronoff, G., Knepp, T., Pippin, M., Allen, D., Twigg, L., Swap, R., Tzortziou, M.,
508 Thompson, A. M., Stauffer, R. M., Wolfe, G. M., Flynn, J., Pusede, S. E., Judd, L. M., Moore, W., Baker, B. D., Al-
509 Saadi, J., and McGee, T. J.: The Ozone Water–Land Environmental Transition Study: An Innovative Strategy for
510 Understanding Chesapeake Bay Pollution Events, *Bull. Am. Meteorol. Soc.*, 100, 291–306,
511 <https://doi.org/10.1175/BAMS-D-18-0025.1>, 2019.
- 512 Wesely, M. L.: Parameterization of surface resistances to gaseous dry deposition in regional-scale numerical
513 models, *Atmos. Environ.*, 41, 52–63, <https://doi.org/10.1016/j.atmosenv.2007.10.058>, 1989.
- 514 Xiao, X., Cohan, D. S., Byun, D. W., and Ngan, F.: Highly nonlinear ozone formation in the Houston region and
515 implications for emission controls, *J. Geophys. Res. Atmospheres*, 115, <https://doi.org/10.1029/2010JD014435>,
516 2010.
- 517 Yu, S., Mathur, R., Pleim, J., Pouliot, G., Wong, D., Eder, B., Schere, K., Gilliam, R., and Trivikrama Rao, S.:
518 Comparative evaluation of the impact of WRF–NMM and WRF–ARW meteorology on CMAQ simulations for O₃
519 and related species during the 2006 TexAQS/GoMACCS campaign, *Atmospheric Pollut. Res.*, 3, 149–162,
520 <https://doi.org/10.5094/APR.2012.015>, 2012.
- 521 Zhang, C., Wang, Y., and Hamilton, K.: Improved Representation of Boundary Layer Clouds over the Southeast
522 Pacific in ARW-WRF Using a Modified Tiedtke Cumulus Parameterization Scheme, *Mon. Weather Rev.*, 139,
523 3489–3513, <https://doi.org/10.1175/MWR-D-10-05091.1>, 2011.
- 524